

Sea Ice - Atmosphere Interaction

Application of Multispectral Satellite Data in Polar Surface Energy Flux Estimates

K. Steffen, J. Key, J. Maslanik, A. Schweiger
Cooperative Institute for Research in Environmental Sciences
Division of Cryospheric and Polar Processes
Campus Box 216, University of Colorado at Boulder

NAGW - 2158

Annual Progress Report
to
National Aeronautics and Space Administration

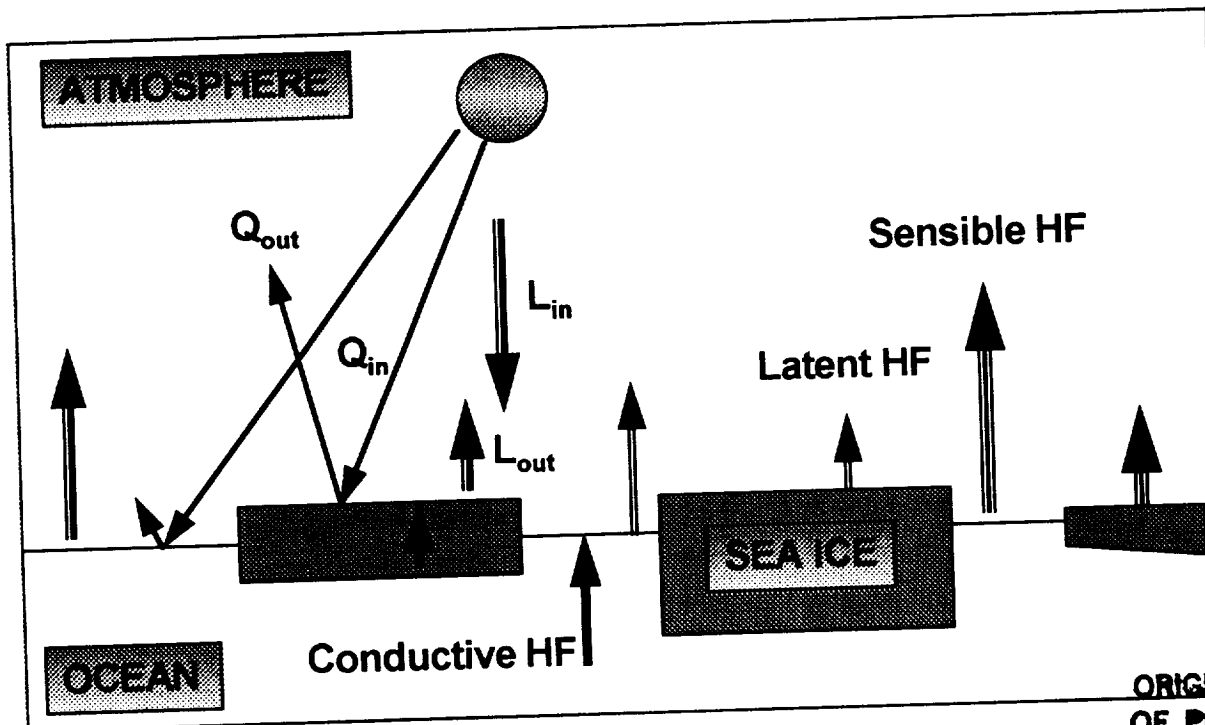
April 1993

N93-28137

Unclas

G3/46 0161910

(NASA-CR-193027) SEA
ICE-ATMOSPHERIC INTERACTION:
APPLICATION OF MULTISPECTRAL
SATELLITE DATA IN POLAR SURFACE
ENERGY FLUX ESTIMATES Annual
Progress Report (Colorado Univ.)
22 p



ORIGINAL PAGE IS
OF POOR QUALITY

TABLE OF CONTENTS

SUMMARY	1
1. ARCTIC CLOUDS AND RADIATION	2
1.1 ISCCP and Surface-Based Cloud Amounts	2
1.2 Radiative Fluxes Estimated from the ISCCP Cloud Data	3
1.3. Radiative Fluxes and Cloud Forcing	7
2. SNOW AND ICE ALBEDO	8
2.1 Calibration of AVHRR Channel 1 and 2	8
2.1.1 Objectives	8
2.1.2 AVHRR calibration	8
2.1.3 Surface and planetary narrow-band albedo	8
2.1.4 Conclusions	10
2.2. Spectral Reflectance	10
2.2.1 Hemispheric Reflectance	10
2.2.2 Anisotropic Reflectance	10
2.2.3 Directional hemispheric reflectance	12
2.3 Comparison of Two Satellite-Derived Albedo Data Sets	12
3. LEADS AND MODELING	15
3.1 Effect of Measurement Scale on Turbulent Fluxes from Leads	15
3.2 Modeling	16
4. REFERENCES	18
5. Publications Supported by NAWG-2158	19
5.1 Reviewed Literature	19
5.1 Reports, Workshop Proceedings	19
5.3 Thesis	20

SUMMARY

This is the third annual report on: Sea Ice-Atmosphere Interaction - Application of Multispectral Satellite Data in Polar Surface Energy Flux Estimates.

The main emphasis during the past year was on: radiative flux estimates from satellite data; intercomparison of satellite and ground-based cloud amounts; radiative cloud forcing; calibration of AVHRR visible channels and comparison of two satellite derived albedo data sets; and on flux modeling for leads.

The highlights can be summarized as following:

- Satellite cloud amounts are generally 5 - 35 % less than observed values over the entire Arctic.
- Shortwave and longwave fluxes at the surface were modeled from satellite data on a monthly basis for the entire Arctic. Net longwave flux was found to be negative throughout the year with a minimum value of -70 Wm^{-2} in the month of May.
- Regional variations in radiative fluxes were discussed and related to variations in cloud amount.
- Seasonal variations of shortwave-, longwave- and net-radiation cloud forcing at the surface were computed; positive net forcing values of 65 Wm^{-2} were found for October through January, and the net cloud forcing was negative for the months May through August.
- Using *in situ* radiosonde measurements narrow-band surface albedo values from AVHRR channels 1 and 2 can be estimated with an accuracy of 2 %, and 14 % respectively. A large discrepancy between modeled and observed radiance in AVHRR channel 2 is believed to result from a satellite sensor drift.
- Albedo values as derived from two different satellite data sets show good agreement in spatial patterns for the entire Arctic. Albedo values derived from ISCCP were lower by 0.1 (10 %) compared to a manual DMSP visible band analysis.
- Relationship between satellite foot prints and averaged turbulent fluxes was established for leads. The turbulent flux as derived from a 80 m field of view (FOV) decreases by 45 % for a satellite footprint of 640 m FOV.
- Narrow leads have been found to be more effective in turbulent flux transfer than wide leads of the same aerial extent.

Officially the three year project has ended in April 1993. We have extended this project at no-cost through December 1993 to complete the analysis and parameterization of energy flux measurements over different ice thickness types. Sensible and latent heat fluxes were measured by K. Steffen in Lancaster Sound during the two winters 1979 and 1981. This data set will now be analyzed by T. DeMaria (supervisor: K. Steffen). The results from this study will be crucial for the discussion of satellite-based turbulent flux estimates. So far no *in situ* flux measurement has been published for Arctic conditions throughout an entire winter (November through February). The final results of this study will be summarized and presented as a final report in early 1994. The main emphasis will be a comparison of different flux components for different ice thicknesses as compared to modeled results based on mean climatology.

1. ARCTIC CLOUDS AND RADIATION

Jeffrey Key and Axel Schweiger

1.1 ISCCP and Surface-Based Cloud Amounts

The International Cloud Climatology Project (ISCCP) is now producing a global cloud product (Rossow et al., 1988). How valid are the reported quantities in the Arctic? This question is critical if we are to use this data product for studies of Arctic climate, for example in the estimation of radiative fluxes as described in the next section. As a first step in determining the validity of these data we have compared the satellite-based cloud amounts to surface-based observations. However, there are many questions concerning the validity of the surface-based cloud amounts as well, so it is not possible to draw conclusions in an absolute sense about either data set. Only a summary of the results is presented here; for more details see Schweiger and Key (in press).

The comparison is made with monthly cloud statistics from an atlas of global cloud cover compiled by Warren et al. (1988; hereafter WAR). Cloud observations from ships for 1951-1981 form the basis for the ocean area atlas. Since there is no direct overlap between the ISCCP and the WAR data sets, only monthly statistics were compared. Interannual variability of monthly cloudiness is small, in the range of 5% for July and up to 8% in January of the four ISCCP years 1983 to 1990, so that errors due to non-overlapping climatologies should be of a lower magnitude than the other potential error sources.

Figure 1 shows the annual variation of total cloud amounts in the ISCCP-C2 and WAR data sets for the region north of 62.5° latitude. Two separate cloud amounts are given for the ISCCP-C2 set: the total cloud amount reported in the ISCCP-C2 data set and marginal cloud amount. The total cloud includes the marginal cloud. Marginal cloud amounts are derived in the ISCCP procedure through the application of a different threshold and represent the first derivative of cloud amount with respect to the threshold. These marginally cloudy pixels display radiance's that are near the clear sky radiance's and occur primarily in areas of broken cloudiness and where the contrast between cloudy and clear conditions is low. Such conditions prevail in the polar regions and the marginal cloud amount is presented as an indicator of the level of uncertainty in the thresholds. As can be seen from Figure 1, this level of uncertainty is greater during winter.

The satellite cloud amounts are generally 5 - 35% less than the surface observations over the entire Arctic. However, regional differences may be as high as 45%. During July the surface-based cloud amounts for the central Arctic are 40% greater than the satellite-based values. In winter the ISCCP climatology in the central Arctic agree to within 10% of the surface observations. While satellite-derived cloudiness during summer seems to reflect the conservative approach of the ISCCP algorithm and probably represents an underestimate, there is considerable uncertainty with respect to the winter cloudiness. Ice crystal precipitation could account for the unexpectedly high winter ISCCP cloud amounts.

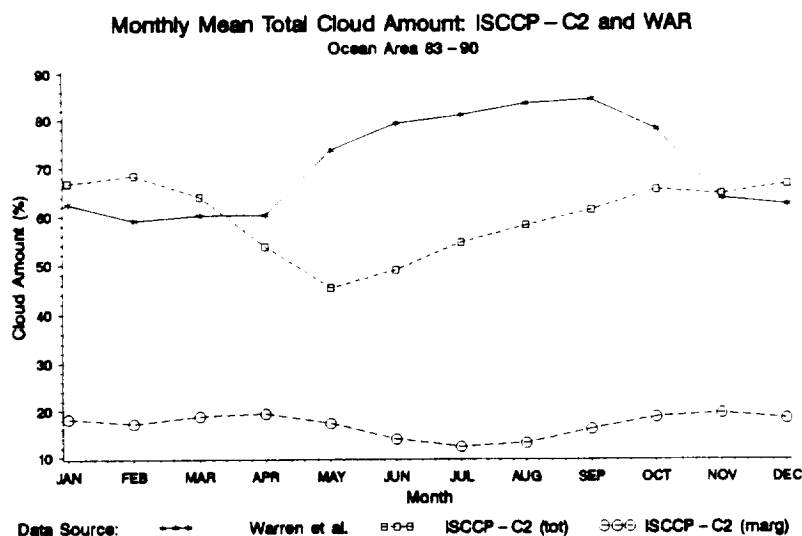


Fig. 1: Annual cycle of total cloudiness in the Arctic (north of 62.5° N latitude) from the ISCCP-C2 and WAR data sets. ISCCP data are for 1983-1990; WAR data cover the period 1951-1981.

1.2 Radiative Fluxes Estimated from the ISCCP Cloud Data

Information on radiative fluxes in the Arctic is sparse and originates mainly from a small number of ice islands coastal stations. More detailed information with significant spatial coverage cannot be expected within the next 10-20 years. In order to quantify the Arctic radiation balance for large-scale process studies such as sea ice modeling experiments as well as for comparison with GCM modeling studies, we must rely on satellite remote sensing techniques which provide the only source of data with sufficient spatial and temporal coverage. A data set of monthly Arctic Ocean radiative fluxes at the surface and top of the atmosphere has been compiled for the years 1983-1986 (Schweiger and Key, 1992). This "climatology" will provide an alternative to prior estimates and incorporates the most recent satellite-derived data sets.

Radiative fluxes are computed using the ISCCP-C2 data set as the main source of information for radiatively important atmospheric and surface properties. The ISCCP-C2 data set is a compilation of monthly statistics from the 3-hourly ISCCP C1 data set and contains information on satellite-derived cloud fraction, atmospheric profiles of temperature, water vapor and ozone, surface temperature and reflectivity, cloud top pressure and temperature, and cloud optical depth. The compilation of this data set is an ongoing effort, but only data covering the period July 1983 to December 1986 are used in this study. This data set provides global coverage from a variety of sensors on a 250 by 250 km analysis grid. For the polar regions the data set consists entirely of data from the AVHRR and TOVS instruments on board the NOAA satellites. The compilation of this data set involves a large number of processing steps; for more detail the reader is referred to Rossow et al. (1988).

The radiative transfer model used to calculate radiative fluxes in this study was modified from Tsay et al. (1988) by replacing the discrete ordinate solution of the radiative transfer equation with a delta-Eddington two-stream approximation for short wave calculations and a hemispheric

mean two-stream approximation with internal source function for long wave calculations. Gas absorption for water vapor, ozone, CO₂ and oxygen is parameterized using an exponential sum fitting technique with 24 bands at varying intervals without overlap for the shortwave region, and 9 bands at 200 cm⁻¹ intervals including overlap of gases for the longwave region. Cloud single scattering properties are parameterized as a function of the effective radius and liquid water concentration. Clouds are represented as Mie-scattering layers of variable thickness. Cloud physical height and optical thickness are set to the values reported in the ISCCP data set. Cloud physical thickness is calculated from the above parameterization with effective radius of 10 μm and a liquid water concentration of 0.2 gm⁻³. These values were chosen to be consistent with the ISCCP retrieval algorithm. During winter no cloud optical thickness is reported in the ISCCP data set and mean summer values are used instead. For each grid cell separate calculations are performed for cloud free and cloudy conditions. Results are linearly averaged with the fractional area of cloud and clear sky as weights.

In order to calculate radiative fluxes, reflectivity or emissivity need to be specified for each of the spectral bands used in the radiative transfer scheme. Consistent with the ISCCP analysis, emissivity is assumed to be unity. Spectral albedo in 24 bands must be estimated from the single channel reflectance reported in the C2 data set (0.6 μm). The problem is complicated by the fact that a variety of surface types may exist within each cell so that the proper mixture must be determined before reflectance's can be assigned. The possible surface types are: open water, melt ponds, bare ice, and snow-covered ice with either 300 μm or 1000 μm snow grain size. The spectral albedo for these surfaces are in part extracted from the literature and in part computed using a 4-stream model analogous to the development of Warren and Wiscombe (1981). For the modeled snow albedo, snow grain size is season-dependent. A soot content of 0.2 ppmw, consistent with the amounts necessary to match measured albedo by Grenfell and Maykut (1977), was used. The albedo at the lower boundary, the snow/ice interface was set to the spectral albedo of ice from which the snow has been removed. The snow-depth in the non-melt season was assumed to 40 cm, a value typical for early May. Spectra for melting first and second year ice, as well as melt ponds are taken from Grenfell and Maykut (1977).

For the baseline case calculations were conducted for all ocean areas north of 62.5°N. Total aerosol optical depth is set to 0.06 and does not vary with season or place. Downwelling shortwave radiation increases from February to a June maximum of 276 Wm⁻² (Fig. 2). Downwelling longwave radiation during summer is of a similar magnitude but has a maximum of 280 Wm⁻² a month later in July (Fig. 3). Variation in downwelling longwave radiation is small from November through May and the minimum occurs in April when air temperatures have begun to rise and cloud amount decreases from winter to spring. While incoming shortwave radiation increases and decreases monotonically to and from the June maximum, downwelling longwave radiation shows a rather abrupt jump of 70 Wm⁻² from May to June. Net longwave fluxes are negative (loss to the surface) throughout the year. Maximum losses of 70 Wm⁻² occur during May when rising surface temperatures coincide with a minimum in cloudiness. While the annual variation is small, summer longwave losses at the surface are greater than during winter by about 20 Wm⁻². Shortwave gains exceed longwave losses from April through September and the net surface radiation balance varies from a minimum in December/February of 33 Wm⁻² to a maximum in July of 112 Wm⁻². This maximum occurs one month after the maximum in downwelling shortwave radiation and is caused mainly by a drop in albedo during this time of the year.

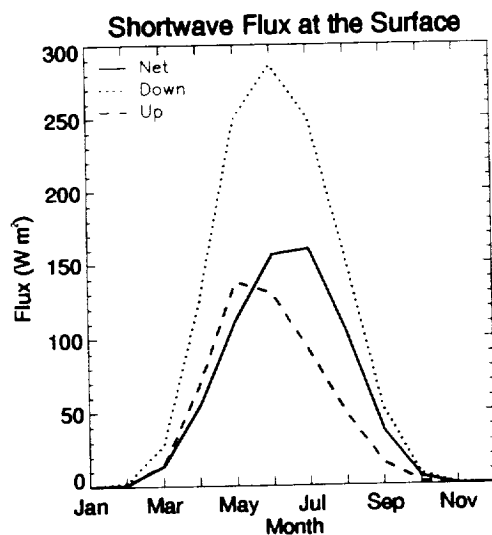


Fig. 2: Annual cycle of shortwave fluxes (Wm^{-2}) for ISCCP baseline case.

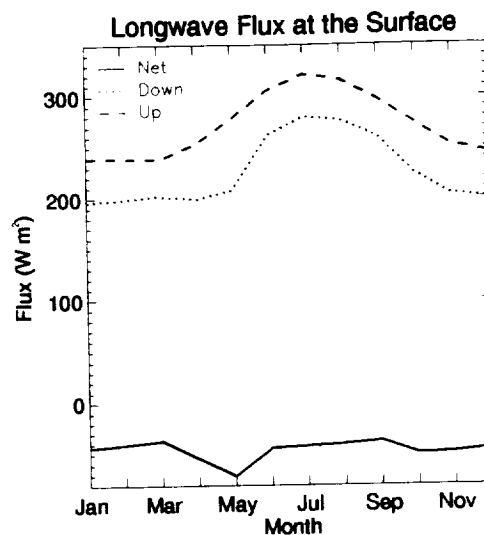


Fig. 3: Annual cycle of longwave fluxes (Wm^{-2}) for the ISCCP baseline case.

The spatial variability was also examined (Fig. 4 and 5). In March the central Arctic regions receive increasing southward up to 150 Wm^{-2} in the Bering Sea area. A modulation of the solar zenith angle effect by cloud amount is apparent in the Greenland/Norwegian Seas area, where cloudiness is usually greater than in other regions of the Arctic. In April this pattern persists, but downwelling fluxes have increased by about 100 Wm^{-2} for the areas north of 70° with a latitudinal gradient of 100 Wm^{-2} similar to the one found in March. By May, when incoming solar radiation at the top of the atmosphere varies little with latitude, cloud amount becomes the dominant factor determining downwelling shortwave radiation at the surface. Since the ISCCP data set reports fewer clouds in the central Arctic than elsewhere, this region receives more solar radiation (300 Wm^{-2}) than other areas of the Arctic. The minimum again occurs in the Greenland/Norwegian Seas area where cloud amounts are persistently high. In June and July, downwelling shortwave patterns vary little over most of the Arctic region with downwelling fluxes in the order of $300\text{--}325 \text{ Wm}^{-2}$ and 275 Wm^{-2} respectively. A steep gradient can again be observed in the Greenland/Norwegian as well as the Barents Seas, where summer cloud amounts of 80% reduce incoming shortwave radiation substantially. In these areas summer ice concentrations, and therefore aeri ally averaged albedo, are lower. Since clouds reduce downwelling shortwave radiation more effectively over lower albedo surfaces, the combination of greater cloud amounts with lower surface albedo leads to downwelling shortwave fluxes as low as 150 and 125 Wm^{-2} in June and July over the Norwegian sea. In August, the solar zenith angle-related concentric pattern redevelops and cloudiness has a secondary effect on the spatial distribution of shortwave fluxes.

Downwelling longwave fluxes show very little variation over most of the Arctic and are on the order of 175 Wm^{-2} from November through April. A strong increase up to 300 Wm^{-2} can be found over the Norwegian, Greenland and Barents Seas areas. This gradient, following roughly the Greenwich meridian is also fairly constant for these month and is again caused by the greater cloudiness over these areas. In May the peripheral seas, because of rising temperatures, begin to receive greater amounts of longwave radiation (200 Wm^{-2}), while the central Arctic remains at

the 175 Wm^{-2} level. In June a sudden jump to 250 Wm^{-2} with little variation over the central areas occurs, and the maximum is reached in July with 275 Wm^{-2} over most of the Arctic Ocean and the peripheral seas. In August this pattern persists at approximately the same level, before values drop again, most drastically in the central Arctic.

Despite significant uncertainties in accuracy, the ISCCP data set for the first time provides an opportunity to calculate radiative surface fluxes and cloud forcings from satellite at a spatial and temporal resolution suitable for sea ice modeling experiments. The accuracy and potential errors of the calculated fluxes are under investigation through comparisons with surface measurements and sensitivity studies.

Downwelling Shortwave Fluxes at the Surface
June, 1984-90

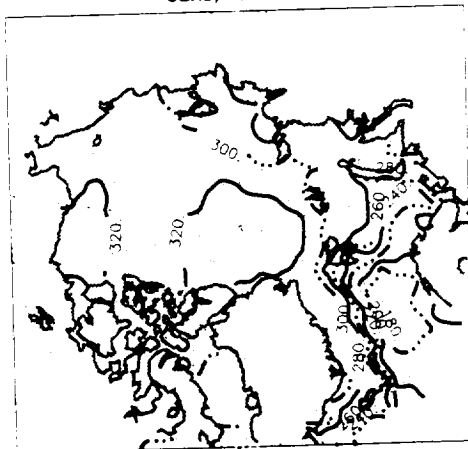


Fig 4: Spatial variability of downwelling shortwave fluxes (Wm^{-2}) for June 1984 - 1990 as derived from ISCCP

Downwelling Longwave Fluxes at the Surface
January, 1984-90



Downwelling Longwave Fluxes at the Surface
June, 1984-90



Fig 5: Spatial variability of downwelling longwave fluxes (Wm^{-2}) for January and June 1984 - 1990 as derived from ISCCP

1.3. Radiative Fluxes and Cloud Forcing

Information on radiative fluxes in the Arctic is sparse and originates mainly from a small number of ice islands and coastal stations. The monthly cloud data product of the International Cloud Climatology Project (ISCCP) has been used to estimate Arctic radiative fluxes and cloud forcing at the surface and top of the atmosphere. An example of the results is shown in Figure 6, which gives the shortwave, longwave, and net cloud forcing at the surface. Throughout much of the year the presence of cloud covers tends to warm the surface. During summer, however, clouds significantly decrease the downwelling shortwave radiation and cool the surface. Despite significant uncertainties in accuracy, the ISCCP data set for the first time provides an opportunity to calculate radiative surface fluxes and cloud forcings from satellite at a spatial and temporal resolution suitable for sea ice modeling experiments. The accuracy and potential errors of the calculated fluxes are under investigation through sensitivity studies and by comparisons with surface measurements.

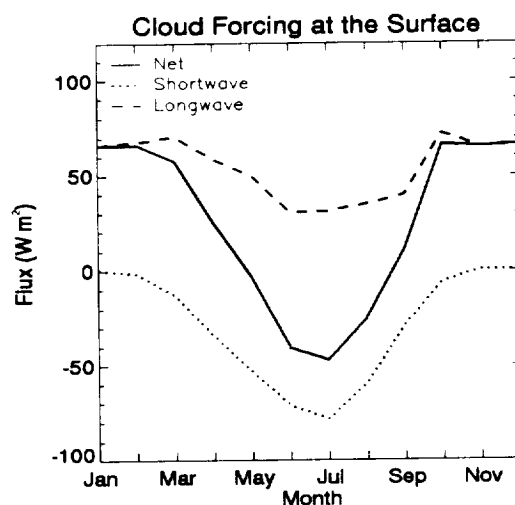


Fig. 6: Shortwave, longwave, and net cloud forcing at the surface in the Arctic. Data are computed from the ISCCP monthly cloud product for the years 1983-1990.

2. SNOW AND ICE ALBEDO

Konrad Steffen, Axel Schweiger and Jeffries Key

2.1 Calibration of AVHRR Channel 1 and 2

2.1.1 Objectives

To discuss the accuracy of the satellite derived reflectance values, in situ spectral reflectance measurements were used to calibrate the Advanced Very High Resolution (AVHRR) channel 1 and 2. The calibration procedure used ground based and atmospheric measurements from the ETH/CU research station on the Greenland ice sheet. The accuracy assessment of satellite derived reflectance is needed to estimate the confidence level for the parameterization of surface energy flux components as derived from satellite data.

2.1.2 AVHRR calibration

NOAA-11 AVHRR LAC data (level 1B) was processed for the two visible channels. The level 1B format includes navigation and calibration information for the images (Lauritson et al., 1979). Small registration errors are present in the resulting images that are removed by linearly nudging the images onto a map grid. With this approach the registration errors can then be reduced to $\pm 1/2$ pixel. The navigation of the data was mapped to a polar stereographic projection with a 1-kilometer per pixel resolution. The resolution of the scan spot from the AVHRR instrument varies from 1.1 kilometer at nadir to about 6.8 kilometers at a scan angle of 55 degrees. This is not a linear function; a scan angle of 30 degrees results in a pixel resolution of 1.5 km.

2.1.3 Surface and planetary narrow-band albedo

Calibration of the AVHRR imagery is channel dependent. For channel 1 and 2 pre-launch values were used which convert digital numbers (DN) to percent albedo (Brown, 1988). For each pixel in the image the solar zenith angles were computed and cosine corrections were applied.

The planetary narrow-band albedo for AVHRR channels 1 and 2, measured on May 23, 1991, were compared against ground based values measured with the portable spectroradiometer on the Greenland ice sheet (ETH/CU camp, 69° 34'N, 49° 17'W, 1155 m a.s.l.). An integration sphere was mounted in front of the optical head for hemispheric measurements, directed towards the zenith and perpendicular to the ground for the calculation of spectral snow reflectance. The snow was less than one day old, with grain sizes between 0.1 - 0.2 mm in diameter. The prevailing air temperature was well below freezing. In addition, broadband global radiation, diffuse and reflected shortwave radiation were measured with a set of pyranometers as part of the ongoing radiation balance experiment at the ETH/CU-Camp. The broadband albedo values derived from the pyranometers was 84.3 %. The spectrally-integrated reflectance for the same spectral region was 82.9 %. This experiment shows that broadband albedo measurements from pyranometer and spectroradiometer can be achieved within 0.7 % accuracy.

The atmospheric absorption and scattering was modeled using the radiative transfer code LOWTRAN 7. This work was performed by Mr. Marcel Häfliger, ETH-Z. Two different model

runs were performed: (a) using the in situ radiosonde profile measurements of temperature and humidity as input data, and (b) using the standard sub-arctic atmosphere. The narrow-band albedo at the top of the atmosphere (a_p) was then calculated by integrating over the AVHRR spectral band-width (λ_1, λ_2), as following:

$$\int [S(\lambda)\Phi_i(\lambda)\tau(\lambda)a_g(\lambda)]d\lambda / \int [S(\lambda)\Phi_i(\lambda)]d\lambda$$

where $S(\lambda)$ is the solar irradiance at the top of the atmosphere, $\Phi_i(\lambda)$ is the spectral response function of the AVHRR channel ($i=1,2$), $a_g(\lambda)$ is the narrow-band reflectance at the ground, and $\tau(\lambda)$ is the calculated spectral transmission for two path lengths: (a) between the top of the atmosphere and the surface, and (b) between the surface and the satellite. The integration was done for both AVHRR channels with (a) radiosonde profile data and (b) standard sub-arctic atmosphere (Tab. 1). The difference between measured (AVHRR) and calculated (spectroradiometer and LOWTRAN) narrow-band planetary albedo for channel 1 is 0.5% using radiosonde profile data in the LOWTRAN 7 model. Using the standard sub-arctic atmosphere in the LOWTRAN model, the difference increased to 2.9%. For AVHRR channel 2 the calculated and measured narrow-band albedo values differ by approximately 9%.

Surface narrow-band albedo a_g can also be derived from planetary narrow-band albedo a_p values as following:

$$a_g = a_p / [\tau_{(\text{sun-surface})}(\lambda) \tau_{(\text{surface-satellite})}(\lambda)]$$

The transmission values were calculated using the radiative transfer model which accounts for the intrinsic atmospheric reflectance due to the Rayleigh and aerosol scattering of the standard sub-arctic atmosphere. The surface narrow-band albedo values derived from the AVHRR planetary albedo are given in Table 2. The differences have the same order of magnitude for the calculated planetary narrow-band albedo which is not surprising as both computations use the LOWTRAN 7 model.

Table 1: Narrow-band albedo values for AVHRR channels 1 and 2 as measured by AVHRR at the top of the atmosphere (a_p = planetary narrow-band albedo), and calculated using ground-based spectrometer values a_g and radiative transfer modeling.

AVHRR Channel	a_p AVHRR	calculated a_p with radiosonde atm.	calculated a_p with standard atm.	a_g Spectrometer
1 (580-680 nm)	68.8%	67.5%	65.5%	91.6%
2 (725 - 1100 nm)	56.1%	65.2%	64.5%	81.0%

Table 2: Narrow-band surface albedo values a_g compared against calculated surface narrow-band albedo from AVHRR channels 1 and 2 using transmission coefficients $\tau_1(\text{sun-surface})$, and $\tau_2(\text{surface-satellite})$.

AVHRR Channel	a_g Spectrometer	calculated a_g with radiosonde AVHRR	calculated a_g with standard atm. AVHRR	τ_1	τ_2
1 (580-680 nm)	91.6%	93.3%	95.1%	0.825	0.895
2 (725 - 1100 nm)	81.0%	69.3%	70.3%	0.878	0.922

2.1.4 Conclusions

Standard sub-arctic aerosol values were used for the computation of aerosol scattering as atmospheric profile measurements were not available. This might explain in part the discrepancies between measured and modeled surface albedo values. Aerosol content can vary with time and space significantly which can reduce the reflectance by several percents. Assuming that the radiative transfer model is correct, we can speculate that a major drift in AVHRR channel 2 has occurred since the launch of NOAA 11 (November, 8, 1988). For the visible channel of NOAA 9 degrading rates of up to 6 % per year were reported (Staylor, 1990). This case study should be judged as a preliminary analysis, as more cases have to be compared for a statistical analysis. In addition, LOWTRAN 7 derived spectral transmission values have to be validated to separate the modeling error from sensor drift.

Narrow-band surface albedo values can be estimated from AVHRR channel 1 and 2 measurements with an accuracy of 2%, 14% respectively using LOWTRAN 7 radiative transfer modeling and radiosonde profile information. More case studies will be analyzed to discuss this technique in more depths and to derive statistically significant values.

2.2. Spectral Reflectance

2.2.1 Hemispheric Reflectance

Hemispheric spectral albedo was measured for five different snow grain size ranges (Table 3, Fig. 7). The largest spectral reflectance in the visible spectrum was found for very new snow. In the near infrared region (900 - 1500 nm) the reflectance depends on the soot content, a parameter not measured in situ during the field experiment. Based on the spectral characteristics of different snow surfaces, satellite and aircraft measurements with high spectral resolution have the potential for classifying the different snow facies.

Table 3: Snow properties for different snow types given in Figure 7

Snow Type	Age	Grain Size (mm)	Solar Zenith Angle
Dry Snow	2 hours	0.5	50
Dry Snow	1 day	0.1-0.2	50
Dry Snow	3 days	0.1-0.3	50
Wet Snow	-	1.0	50
Wet Snow	-	2.0-5.0	68

2.2.2 Anisotropic Reflectance

The anisotropic reflectance factor (ARF) was calculated based on the field measurements for dry snow with grain sizes varying between 0.1 - 0.3 mm (diameter). Figure 8 shows the ASF for a reflectance angle of 85° and a solar zenith angle of 71°. The results are in good agreement with earlier measurements taken in the spectral range 400 - 500 nm (Steffen, 1987). The measurements show that dry snow can be treated as an Lambertian reflector with minor spectral dependency. The

results for wet snow have not fully been analyzed yet, but they clearly show a strong specular reflectance dependency on the azimuth angle. The wet snow ARF values will be needed for the conversion of satellite-based directional-spectral reflectance to albedo.

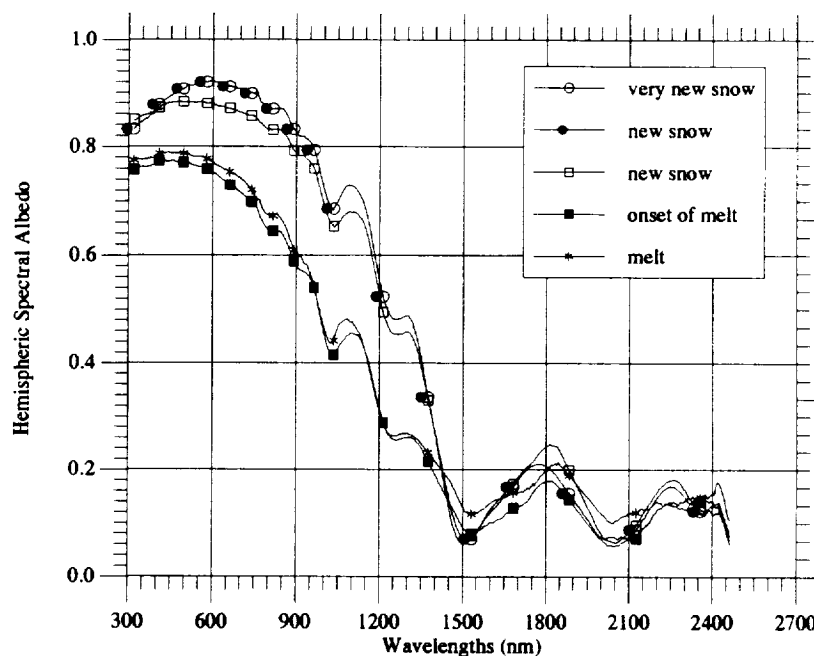


Fig. 7: Hemispheric spectral albedo for very new snow, new snow, onset of melt, and melting snow surface in the range 300 - 2500 nm. Snow properties and solar zenith angles for each measurement is given in Table 3.

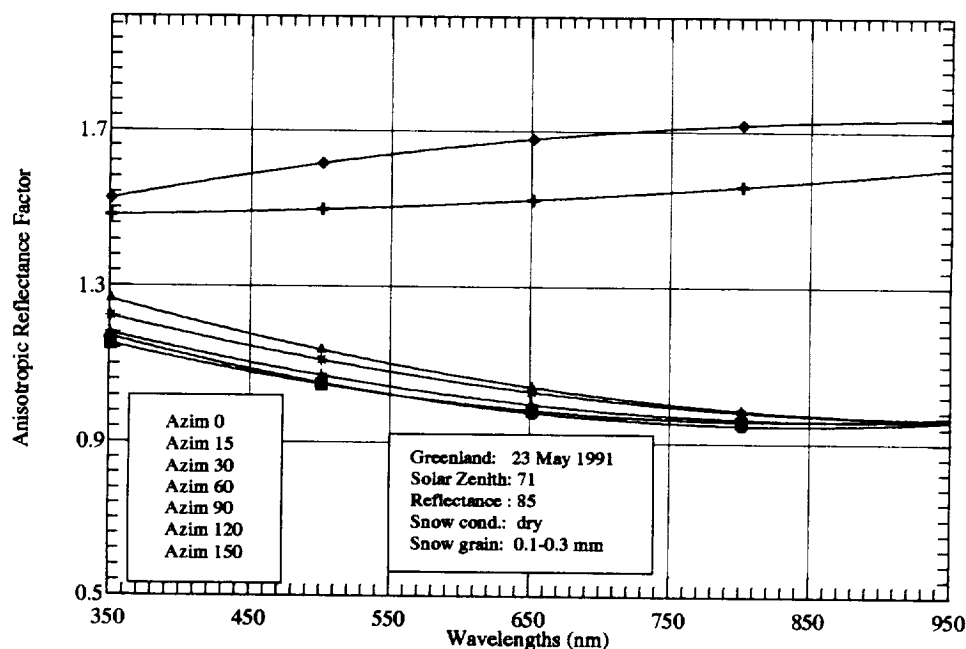


Fig. 8: Anisotropic reflectance factor for seven different azimuth angles, a reflectance angle of 85°, and a solar zenith angle of 71°. The snow was dry with grain radii varying between 0.1 - 0.3 mm.

2.2.3 Directional hemispheric reflectance

Bidirectional Distribution Reflectance Function (BDRF) was modeled replacing the two-stream approach as discussed by Warren and Wiscome (1981) with a discrete-ordinate solution (48 streams). The model assumes Mie-scattering of optically equivalent ice spheres. Small amounts of carbon soot are included in the medium and are needed to achieve a match between measured and modeled reflectance's in the visible region. Presently modeling results assume a single homogenous layer of snow but multi-layer calculations are also possible.

The model results were compared with field measurements as shown in Figure 9. In general there is a good agreement if a soot amount of 0.30 ppmw were used. This soot amount seems rather high for the Greenland region, however, in situ measurements are missing and can not confirm this assumption. If the model run was performed with 0.00 ppmw soot amount, the spectral reflectance in the visible range (0.3 - 0.8 μm) was approximately 0.1 higher than the in situ measurement.

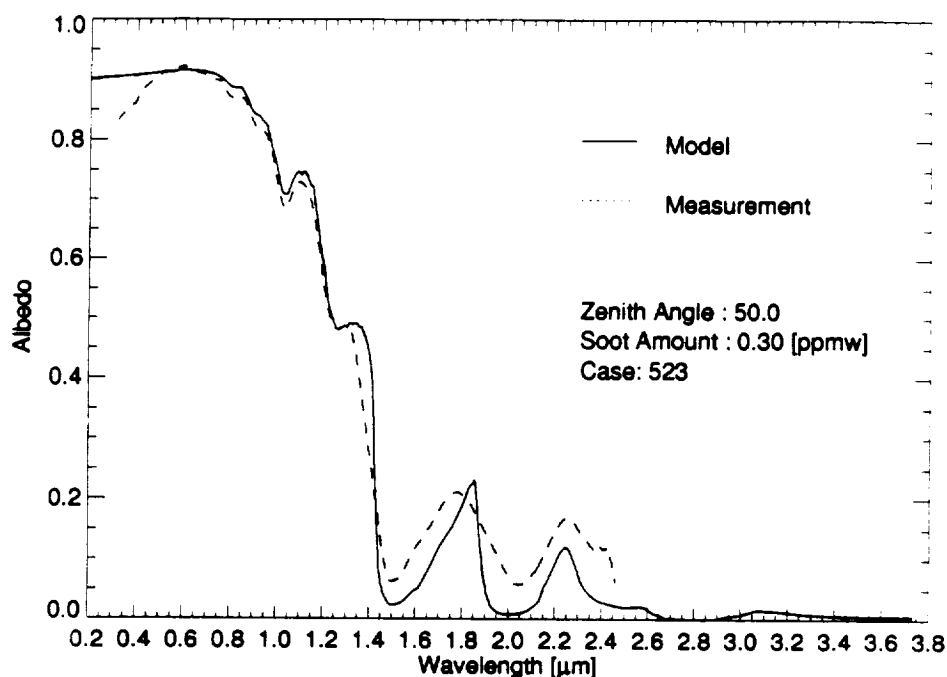


Fig. 9: Directional hemispheric albedo of snow from with discrete-ordinate model versus ground measurement for a dry snow surface with a mean grain size of 0.1 mm. For the model computation a soot amount of 0.3 ppmw was assumed.

2.3 Comparison of Two Satellite-Derived Albedo Data Sets

Variations in the surface albedo of the Arctic pack ice cover is an important factor in the long-term mass balance and stability of the pack ice. Continued monitoring of albedo is consequently an important component of the "early detection" strategy for identifying global and regional climate changes. Nevertheless, until recently, studies of the Arctic Ocean albedo have been of limited spatial and temporal scope, based largely on observations at drifting stations, fast ice, and during aircraft missions. Other investigators have used these measurements and satellite passive microwave data to estimate regional summer albedo (Robinson et al., 1992).

With the aim of developing a long-term record Robinson et al. (1992) recently developed a ten year data set of parameterized albedo for the entire Arctic Ocean for May through mid-August. Maps of surface brightness charted through manual analysis of visible-band DMSP imagery were converted to parameterized surface albedo. Although lacking radiometric control, this data base (hereafter referred to as the RO92 set) has allowed for definition of the climatological characteristics of albedo. More recently, we have compiled a separate albedo data set, based on the fluxes derived from the ISCCP monthly data set as described in the previous section. We have compared these two data sets for the months of May, June, and July. While providing an evaluation of uncertainties in our current knowledge of Arctic Ocean surface albedo, such a comparison also makes clear problems in the automated extraction of these data, and clarifies aspects of the existing retrieval algorithm in need of further attention.

Results may be summarized as follows. During May, when snow melt is largely confined to coastal regions (Robinson et al., 1992) both data sets show little spatial variability over the central Arctic. The RO92 albedo over the central Arctic tend to be between 0.75 and 0.80 (the latter figure representing the maximum possible parameterized value). By contrast, the ISCCP values over the same regions are lower by about 0.05 to 0.10. Both data sets show a strong gradient of decreasing albedo near coastal regions, especially toward the Norwegian and East Siberian Seas, consistent with the effects of decreasing ice concentrations and coastal snow melt (Robinson et al., 1992). Both data sets also show surface albedo to be lower near the New Siberian Islands. The reduction in albedo near the western portion of the Canadian Arctic Archipelago shown by ISCCP, however, is not depicted in the RO92 analysis.

By June, melt is underway over large areas of the sea ice cover (Robinson et al., 1992) which results in a decrease in surface albedo (Fig. 10). Both data sets show a concentric pattern of surface albedo, with values decreasing from the pole southwards. Serreze et al. (1991) show that this concentric pattern can be related to the climatological distribution of melting degree days. ISCCP albedo, however, again tend to be lower than those reported by RO92. For example, in the central Arctic regions ISCCP tends to be lower by about 0.1.

Albedo continue to decline during July. The concentric pattern observed in both data sets for June is still present. During July the ISCCP and RO92 albedo match very well, except near the pole where ISCCP albedo are now higher than the RO92 values by up to 0.05.

In summary, generally good agreement in the spatial patterns of surface albedo is found between RO92 and ISCCP data sets. While the RO92 data set cannot be considered "ground truth", the similarity between albedo patterns in these two independently-derived products gives a positive outlook for operational retrieval of albedo from satellite data. However, there are systematic differences in the absolute albedo values, with ISCCP albedo being lower during May-June and higher in July. Reasons for these differences presumably reflect the present inadequacies in the ISCCP cloud-clearing algorithm and the simplifications and subjectivity in the RO92 procedures. Because of these uncertainties it is not currently possible to determine which is more correct.

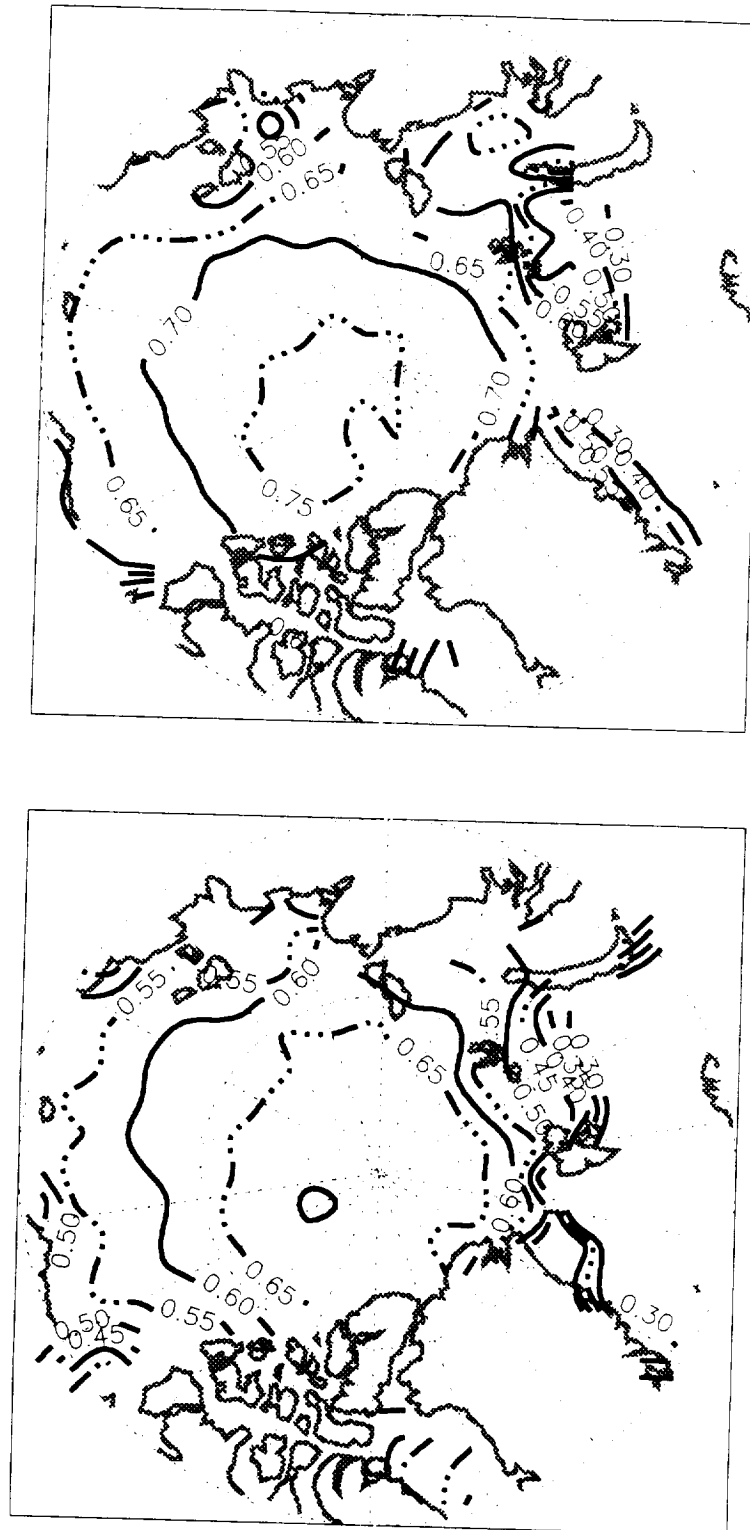


Fig. 10: Mean monthly albedo for June from the RO92 (top) and the ISCCP C2 (bottom) data sets.

3. LEADS AND MODELING

Jim Maslanik and Jeffries Key

3.1 Effect of Measurement Scale on Turbulent Fluxes from Leads

Fractures in the sea ice pack ("leads"), either open or refrozen, are an important component of local scale heat exchange in the Arctic, providing a significant source of heat and moisture to the atmosphere that is as much as two orders of magnitude greater than turbulent energy exchange from thick sea ice. Lead coverage also affects the ice-pack albedo and in turn, the rate of ice melt through the absorption of heat within the open-water leads (Maykut and Perovich, 1987). Modeling studies of the influence of sea ice leads on climate point out the importance of accurately representing lead fraction, which typically defines the proportion of open water within the interior pack ice (Ledley, 1988). Relatively large changes in lead coverage can be related to strong storms in the Arctic (Maslanik and Barry, 1989) and can contribute as a positive feedback to maintaining the strength of these storms. In addition to total lead-covered area, the widths of individual leads affects the rate of heat transfer from the ocean to the atmosphere (Andreas and Murphy, 1986). Unfortunately, relatively little information is available on the numbers, dimensions, and life cycle of leads in the Arctic ice pack. Remote sensing - in particular the use of medium-resolution imagery from polar orbiters such as the NOAA Advanced Very High Resolution Radiometer (AVHRR) - offers the potential to develop a climatology of lead statistics that is well-suited for climate studies and comparison to other remotely-sensed data such as microwave imagery. However, the validity of the retrieved geometrical characteristics of leads - in particular lead widths and area fraction - from medium and low-resolution data is uncertain, so that any estimates of their climatic impact are of questionable utility.

Key et al. (in press) have examined the effects of satellite sensor resolution on lead width distributions, mean lead widths, and total area coverage of leads within an image. It was shown that small leads tend to disappear in the coarser resolution data and large leads "grow" primarily by becoming wider. The total lead fraction decreases as field-of-view increases, roughly following a log-linear relationship. Both the rates and direction of change are, however, closely tied to the threshold used in creating the binary image. Lead orientation distributions also change with increasing pixel size indicating that, in the imagery examined, small leads exhibit different orientations than larger leads.

How do these relationships affect area-averaged estimates of turbulent heat flux? Changes in both the mean lead width and lead-covered area are considered in the calculation of sensible and latent heat flux as a function of fetch (treated here as the lead width), surface temperature, air temperature, and wind speed using the procedure outlined by Andreas and Murphy (1986). In this approach, a bulk Richardson number defines atmospheric stability that controls convective turbulence based on temperature and wind speed. Convective turbulence combines with the mechanical mixing introduced by the step effect of an air mass in equilibrium with thick sea-ice conditions. This air mass is traveling over the physically rough edge of a lead and the considerably warmer open water or thin ice in the lead. The addition of mechanical turbulence introduced by the ice-lead boundary tends to result in a higher rate of heat transfer from smaller leads compared to larger leads. Thus, for a given aerial coverage of leads in an image, a greater number of smaller leads will result in more heat loss to the atmosphere than from a lesser number of larger leads, even though the total amount of open water in the image remains the same. Under the conditions examined by Andreas and Murphy (1986), this decrease in flux as lead

width increases becomes negligible for lead widths greater than about 200 m.

To illustrate the effects of changes in lead statistics using different image fields-of-view, we calculated sensible and latent heat flux using the above approach with a variety of Landsat images successively degraded from a pixel size of 80 m to 160, 320, and 640 m pixel size images. An open-water temperature of -1.8°C , wind speed of 5 m s^{-1} , air temperatures of -28.9°C at a reference height of 2 m, ocean salinity of 34 ppt, air pressure of 1000 mb, and a neutral-stability drag coefficient of 1.49×10^{-3} are used to represent typical mid-winter (January) conditions over the Arctic sea ice pack. Although leads are often covered by thin ice rather than open water and thus have a lower surface temperature than open water, the assumption that the leads are not refrozen and have a surface temperature of -1.8°C is a useful baseline for our calculations. Turbulent (sensible plus latent) heat flux from leads is calculated using the mean lead width at each field of view and then weighted by the aerial coverage of leads for the images to yield an aerielly-averaged heat flux. Turbulent fluxes from open-water leads under these conditions are around 300 Wm^{-2} compared to a flux of nearly 0 from surrounding ice taken to be three meters thick. Thus, lead fraction and lead width dominate the transfer of turbulent heat through the ice pack during winter. Table 4 shows these aerial averages for six MSS images. Since the effect of increasing the fields-of-view in these examples is to decrease the apparent lead fraction, aerielly-averaged fluxes decrease as field-of-view increases. However, as noted earlier, the choice of thresholds can affects both the magnitude and direction of change in lead statistics with changing FOV. If we assume that the lead widths and lead fractions measured using the 80 m FOV imagery are closest to reality, then the errors introduced by using lead widths and lead fraction measured at a 640 m FOV are substantial - averaging 45% over the six images. Since the change in turbulent heat transfer with changing lead width is greatest for smaller leads, those images with smallest mean lead widths at the 80 m FOV (such as Images C and F) are most affected. In the images studied here, where the mean lead width is fairly large, the effect of errors in lead fraction is about five times that of the effect of uncertainty in lead width.

Table 4. Aerially averaged turbulent (sensible and latent) flux (in Wm^{-2}) for typical January conditions as a function of field of view for six MSS images. The percent change in the flux between FOVs of 80 m and 640 m is also shown.

FOV (m)	A	B	C	D	E	F
80	23.5	19.1	17.4	50.7	10.6	15.0
160	22.2	17.7	14.4	47.0	9.7	12.1
320	19.9	16.1	11.7	41.6	8.2	8.9
640	16.7	14.0	7.9	33.7	5.6	5.3
% change	29	27	55	34	47	65

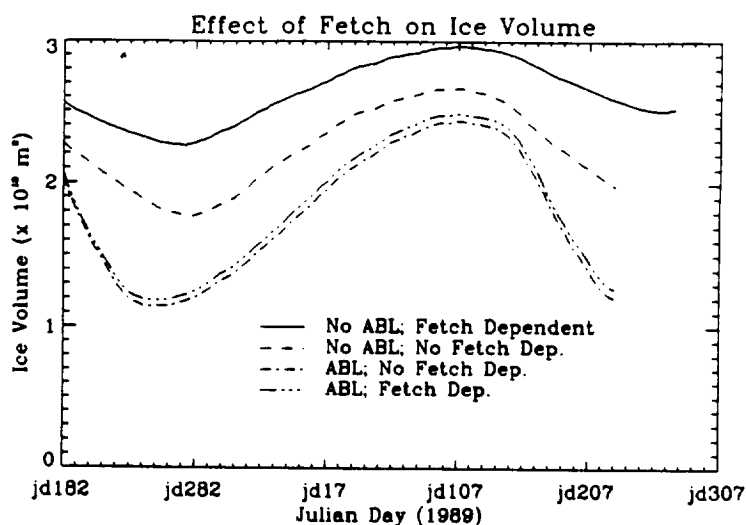
3.2 Modeling

A valuable way of assessing the relative importance of remotely-sensed parameters and of assigning accuracy requirements to remote-sensing algorithms is through numerical sensitivity studies of the ice/atmosphere system. In one example of such studies, we focus on defining the role of ice lead geometry in simulations of the sea ice cover. Low-resolution imagery such as AVHRR and passive microwave data provide information on total open-water area within regions, but are not useful for mapping the widths of individual leads. Leads can be mapped in high resolution imagery such as SAR, but only with considerable effort. However, research has shown that the rate of turbulent heat transfer varies significantly with lead width for leads less than about 100 m.

The question arises, then, as to whether accurate simulations of sea ice require lead width data. To test this and other such sensitivities, we use a sea ice model that simulates the Arctic ice pack, and includes a coupling to the atmospheric boundary layer. This coupling is important in that it allows changes in the ice pack to affect the overlying atmosphere, whereas previous sensitivity studies typically do not allow this feedback. The ice model is run using daily wind fields, climatological ocean currents, snowfall, and cloud properties, and modeled longwave and shortwave radiation. Typically, our model runs for this project use daily forcings for 1989-1991. The effect of lead width is addressed by using a larger bulk heat transfer coefficient for narrow leads.

Results of ice-pack simulations addressing the question of the importance of lead width are summarized in Figure 11. The significance of treating lead width in the model depends on the desired output. Ice growth remains steady as lead width changes in this approach, due to a negative feedback between turbulent heat flux and air temperature. Results show that, when heat from leads is removed from the system (e.g., not allowed to warm the near-surface air), ice volume increases by 17% for the period shown. However, when heat rising from the leads is retained in the boundary layer, the effect of lead width (or the effect of increasing the rate of heat transfer) is 3%. This difference is due to the fact that, although the heat transfer is more efficient from small leads, surface air temperatures are higher, so the rate of heat loss and the resulting ice growth rate, are relatively unaffected. Thus, in terms of ice production in this type of model, the importance of lead width lies somewhere between these two extremes where all heat is removed from the system versus the cases where heat is retained in the atmosphere above leads and sea ice, with no lateral mixing of air over the two surfaces. In terms of atmospheric effects and climate modeling, taking into account the more efficient heat transfer from narrow leads produced mean increases in surface air temperature of about 0.1 C in the central Arctic and approximately 1.2^o C in the seasonal sea ice zones in the extreme case tested here of no air-mass mixing or advection. This difference is due to the proportion of open water in the ice pack, which averaged less than 2% in the central Arctic in these simulations. In particular, these results suggest that in terms of turbulent heat transfer (ignoring effects of lead width on solar heat absorption and lateral melt rates), detailed knowledge of lead width distributions may be of secondary importance. More such experiments are planned to test the sensitivity of the Arctic ice-atmosphere system to other remotely-sensed parameters, as well as to a more realistic situation where lateral mixing of air over leads and ice is permitted.

Fig. 11: A comparison of the effect of including lead width (taken as equal to fetch) in the calculation of turbulent heat flux in simulations of the Arctic ice cover. Lead width parameterized as a function of ice concentration, with heat transferred more efficiently from narrow leads than wide leads. Ice volume represents the sum of all ice in the Arctic and peripheral seas. Simulated ice volumes are shown for the period from 1 Jan. 1989 - 3 Nov. 1990 to represent the seasonal cycle. In the "No ABL" cases, the coupling between the sea-ice surface and the overlying atmospheric boundary layer is turned off, so that surface air temperatures are independent of surface heat flux. In the "ABL" cases, the coupling allows heat from the surface to warm the overlying air to separate equilibrium temperatures over ice and open water.



4. REFERENCES

- Andreas, E.L. and B. Murphy, Bulk transfer coefficients for heat and momentum over leads and polynyas, *J. Phys. Ocean.*, 16(11), 1875-1883, 1986.
- Curry J.A and E.E. Ebert, Annual cycle of radiation fluxes over the Arctic Ocean: sensitivity to cloud optical properties. *Int. J. Climatatology* (in press).
- Brown, S.R., Amendments to NOAA Technical Memorandum 107, Appendix-B for NOAA-H/11, 1988.
- Grenfell, T.C. and G.A. Maykut, The optical properties of ice and snow in the arctic basin. *J. Glaciol.*, 18(80), 445-463, 1977.
- Key, J., J.A. Maslanik, and E. Ellefsen, The effects of sensor field-of-view on the geometrical characteristics of sea ice leads and implications for large-area heat flux estimates. *Remote Sensing Environ.*, in press.
- Lauritson, L., G.J. Nelson, and F.W. Porto, NOAA Technical Memorandum NESS 107, Data Extraction and Calibration of TIROS-N/NOAA Radiometers, 1979.
- Ledley, T.S., A coupled energy balance climate-sea ice model: Impact of sea ice and leads on climate, *J. Geophys. Res.*, 93:15915-15932, 1988.
- Maslanik, J.A. and R.G. Barry, Short-term interactions between atmospheric synoptic conditions and sea ice behavior in the Canada Basin, *Annals Glaciol.*, 12:113-117, 1989.
- Maykut, G.A. and D.K. Perovich, The role of shortwave radiation in the summer decay of a sea ice cover, *J. Geophys. Res.*, 92(C7), 7032-7044, 1987.
- Robinson, D.A., M.C. Serreze, R.G. Barry, G. Scharfen, and G. Kukla, Large-scale patterns and variability of snow melt and parameterized surface albedo in the Arctic Basin, *J. Climate*, 5(10), 1109-1119, 1992.
- Rossow, W.B., L.C. Gardner, P. Lu, and A. Walker, International Satellite Cloud Climatology Project (ISCCP) Documentation of Cloud Data. World Climate Research Programme, WMO/TD-No. 266, 1988.
- Schweiger, A.J. and J. Key, Arctic radiative fluxes and cloud forcing estimated from the ISCCP C2 cloud data set. Proceedings of the Third Conference on Polar Meteorology and Oceanography, American Meteorological Society, Portland, Oregon, 29 Sept - 2 Oct 1992, 13-16, 1992.
- Schweiger, J.A. and J. Key, Arctic Cloudiness: Comparison of ISCCP-C2 and Nimbus-7 Satellite-Derived Cloud Products with a Surface-Based Cloud Climatology. *J. Climate* (in press).
- Schweiger, A.J., M.C. Serreze, and J. Key, Arctic sea ice albedo: a comparison of two satellite-derived data sets. *Geophys. Res. Letters*, 20(1), 41-44, 1993.
- Serreze, M.C., T.L. Dermaria, R.G. Barry and D.A. Robinson, Atmospheric forcings on large-scale patterns of parameterized albedo over Arctic sea ice: case studies for June 1975 and 1988, Proceedings, Fifth Conference of Climate Variations, October 14-18, Denver, CO, Am. Meteor. Soc., 396-399, 1991.
- Staylor, W.F., Degrading rates of the AVHRR visible channel for the NOAA 6, 7, and 9 spacecraft. *J. Atm. and Ocean. Technol.*, 7, 411-423, 1990.
- Steffen, K., Bidirectional reflectance of snow at 500 - 600 nm. IAHS publication, 166, 415-425, 1987.
- Tsay, Si-Chee, K. Stamnes and K. Jayaweera, Radiative Energy Budget in the Cloudy and Hazy Arctic. *J. Atmos. Sci.* Vol.46(7), 1002-1018, 1990.
- Warren, S.G., and W.J. Wiscombe, A model for the spectral albedo of snow II. Snow containing atmospheric aerosols. *J. Atmos. Sci.*, 37, 2734-2745, 1981.

- Warren, S.G., C.J. Hahn, J. London, R.M. Chervin, and R. Jenne, Global distribution of total cloud cover and cloud type amounts over the ocean. NCAR Technical Note TN-317+STR, Boulder, Colorado, 1988.
- Wiscombe, W.J. and S.G. Warren, A model for the spectral albedo of snow. I : Pure snow. *J. Atmos. Sci.*, 3, 72712-2733, 1981.

5. Publications Supported by NAWG-2158

5.1 Reviewed Literature

- Grenfell, T.C., D. Cavalieri, D. Comiso., and K. Steffen, Microwave remote sensing of sea ice: Chapter 14: Consideration for microwave remote sensing for thin ice, ed. F. Carsey, *Geophys. Monograph* 68, 291-230, 1992.
- Häfliger, M., K. Steffen, C. Fowler, AVHRR surface temperature and narrow-band albedo comparison with ground measurements for the Greenland ice sheet, *Annals of Glaciology*, 17, (in press).
- Key, J. and M. Häfliger, Arctic ice surface temperature retrieval from AVHRR thermal channels. *J. Geophys. Res.*, 97(D5), 5885-5893, 1992
- Key, J., J.A. Maslanik, and E. Ellefsen. The effects of sensor field-of-view on the geometrical characteristics of sea ice leads and implications for large-area heat flux estimates. *Remote Sensing Environ.*, in press.
- Maslanik, J. and J. Key. Comparison and integration of ice-pack temperatures derived from AVHRR and passive microwave imagery. *Annals Glaciol.*, 17, in press.
- Schweiger, A.J. and J. Key, Comparison of ISCCP-C2 and Nimbus-7 satellite-derived cloud products with a surface-based cloud climatology in the arctic. *J. Climate*, 5(12), 1514-1527, (in press).
- Schweiger, A.J., M.C. Serreze, and J. Key, 1993. Arctic sea ice albedo: a comparison of two satellite-derived data sets. *Geophys. Res. Letters*, 20(1), 41-44, 1992.
- Seelye, M., K. Steffen, and D. Cavalieri, Microwave remote sensing of sea ice: Chapter 15: Microwave remote sensing of polynyas, ed. F. Carsey, *Geophys. Monograph* 68, 303-309, 1992.
- Steffen, K., J. Comiso, K. StGermain, P. Gloersen, J. Key, and I. Rubinstein, Microwave remote sensing of sea ice: Chapter 10: The estimation of geophysical parameters using passive microwave algorithms, ed. F. Carsey, *Geophys. Monograph* 68, 201-228, 1992.
- Steffen, K., R. Bindshadler, C. Casassa, J. Comiso, D. Eppler, F. Fetterer, J. Hawkins, J. Key, D. Rothrock, R. Thomas, R. Weaver, and R. Welch, Snow and ice applications of AVHRR in polar regions: report of a workshop held in Boulder, Colorado, May 20, 1992. *Annals Glaciol.*, 17, in press.

5.1 Reports, Workshop Proceedings

- Key, J., A.J. Schweiger, and J.A. Maslanik, Arctic radiation forcing fields for dynamic-thermodynamic sea ice models. Report of the Sea Ice Thickness Workshop, NASA Goddard Space Flight Center, 19-21 November 1991, C9-C13, 1992.
- Key, J. and M. Haeffliger, Retrieval of ice surface temperature, outgoing longwave radiation, and cloud cover from AVHRR data. WMO Report on Polar Radiation Fluxes and Sea Ice Modeling, WCRP-62, WMO/TD-No. 442, C22-C28, 1992.
- Serreze, M.C., A.J. Schweiger, and J. Key, Comparison of two satellite-derived albedo data sets for the Arctic Ocean. Snow Watch 92, March, forthcoming.
- Steffen, K., Climatology of the Arctic ocean: Historical data sets, Arctic System Science Ocean-Atmosphere-Ice Interactions Modeling workshop, Report 1, 46-48, 1992.
- Steffen, K. Spectral reflectance of snow. ETH Greenland Expedition, Progress Report 2, eds A. Ohmura. Dept. of Geography, Swiss Federal Institute of Technology, Zürich, 63-69, 1992.
- Steffen, K., and A. Schweiger, Ocean surface energy flux estimates from satellite data in Arctic regions, Marine Technol. Society, Volume II, 434-440, 1992.
- Steffen, K., and A. Schweiger, Application of passive microwave satellite data in Arctic climate research. Glaciological Data, Passive Microwave Research, Univ. of Colorado at Boulder, GD-24, 19-28, 1992.
- Steffen, K., and A. Schweiger, Sea ice retrieval comparison with Landsat satellite and aerial photography of the Bering Sea. 2nd WMO Operational Ice Remote Sensing Workshop, Atmospheric Environmental Service, Vol. 2, 121-130, 1992.
- Steffen, K. and A. Schweiger, DMSP-SSM/I NASA algorithm validation using Landsat satellite imagery. NASA Technical Memorandum 104559, 33-46, 1992.
- Winebrenner, D., J. Key, A. Schweiger, E. Nelson, R. Colony, D. Barber, and E. LeDrew, On links between microwave and shortwave signatures of multiyear sea ice during the onset of melt, Topical Symposium on Combined Optical-Microwave Earth and Atmosphere Sensing, 22-25 March, Albuquerque, NM, 74-77, 1993.

5.3 Thesis

- Schweiger, A., Large scale Arctic radiative fluxes from 1983-1986 modeled from ISCCP-C2 data set. Ph.D. Thesis, Dept. of Geography, University of Colorado at Boulder, pp.218, 1992.